A

Dissertation

On

"Study of Na_2O doped CeO_2 as electrolyte for solid oxide fuel cell application"

A thesis submitted in partial fulfillment

of the requirement for the award of the degree of

Master of Science (Physics)
(2015 - 2017)

Submitted by

Sachin Jaidka

(Registration no. 301504030)

Under the supervision of

Dr. Kulvir Singh

(Professor)

School of Physics and Materials Science
Thapar University, Patiala, Punjab - 147004

July-2017

हर हर

महादेव!!

CERTIFICATE

I hereby certify that the work presented in this thesis report entitled **"Study of N_2O doped CeO_2 as electrolyte for solid oxide fuel cell application"** in the fulfillment of requirement for the award of degree of **Master of Science (Physics)**, submitted in School of Physics and Materials Science, Thapar University, Patiala is an authentic record of the research work carried out under the supervision of **Dr. Kulvir Singh** (Professor and Associate Dean Strategy, School of Physics and Materials Science, Thapar University, Patiala) from January 2017 to July 2017. The results embodied in the thesis have not been submitted in part or full to any other University or Institute for the award of any degree or diploma.

Jaidka

(Sachin Jaidka) **Date: 20 July, 2017**

Registration No. 301504030

It is certified that the above statement made by the student is correct to the best of my knowledge and belief.

(Dr. Kulvir Singh)

(Professor)

School of Physics and Materials Science

Thapar University, Patiala, Punjab

ACKNOWLEDGEMENT

After an intensive period of six months, today is the day: writing this note of thanks is the finishing touch on my dissertation. It has been a period of intense learning for me, not only in the scientific area but also on a personal level. I would like to reflect on the people who have supported and helped me so much throughout this period.

I would first like to thank my thesis advisor **Dr. Kulvir Singh** (Professor, School of Physics and Materials Science) Thapar University, Patiala. The door to Prof. Singh's office was always open whenever I ran into a trouble or had a question about my work or writing. You definitely provided me with the tools that I needed to choose the right direction and successfully complete my dissertation. I would like to thank you for your excellent suggestions, constructive criticism and for all of the opportunities I was given to conduct my research.

I would also like to thank my colleagues from Thapar University for their wonderful collaboration. You supported me greatly and were always willing to help me. I would like to thank my tutors, **Mr. Savidh Khan, Mr. Gaurav Sharma, Dr. Satwinder Singh, Mr. Devender Kumar, Mr. Aayush Gupta, Mr. Santhosh Mahadevan, Mr. P.K. Singh** and last but not the least **Mr. Kaushlendra Pandey**, for their valuable guidance and moral support.

I must also express my very profound gratitude to my friends **Ms. Rajni Sharma, Ms. Shaifali Mehta, Mr. Varun Singhal, Mr. Amit Singh Vig, Ms. Raveena, and Ms. Hima Bhatia** for providing me with unfailing support and continuous encouragement throughout my time of study and through the process of researching and writing this thesis. We were not only able to support each other by deliberating over our problems and findings but also happily by talking about things other than just our work. I would also like to thank **Mr. Pradeep Bhatia** of SAI Labs, Patiala for helping me out with SEM in the last moments.

Finally, I would like to thanks my parents **Sh. Surender Pal and Smt. Usha Jaidka** for supporting me and helping me to live my dreams, you made me a better person and you are the only reason I am standing tall against all the odds in this world with my head held high. This accomplishment would not have been possible without any of you. Thank you very much, everyone!

Sachin Jaidka

Patiala, July 2017

ABSTRACT

In the present study, Na_2O doped CeO_2 has been prepared by solid state reaction method. The samples are sintered at 1300 °C for 12 hours followed by furnace cooling. The synthesized samples are characterized by X-ray diffraction (XRD) for phase confirmation and their volume fractions. UV-Visible spectroscopy, Fourier transform infrared (FTIR) spectroscopy and Impedance spectroscopy are used for optical, structural and conducting properties of the as-prepared samples, respectively. All the samples are crystalline in nature due to sharp peaks present in the XRD patterns. The optical band gap of all the samples lies in the insulating range. CNH-0.05 sample shows highest band gap (~3.21 eV) as compared to other samples. The SEM images show a non-uniform distribution of particles with an average size of ~ 3μm in all the samples. The conductivity of the samples is less than the un-doped samples and lies in the range of 10^{-7} S/cm.

INDEX

List of figures **Page no.**

List of Tables **Page no.**

List of Abbreviations

Alkali fuel cell	AFC
Molten carbonate fuel cell	MCFC
Phosphoric acid fuel cell	PAFC
Proton exchange membrane fuel cell	PEMFC
Solid oxide fuel cell	SOFC
Yttria stabilized zirconia	YSZ
X-ray diffraction	XRD
Fourier transform infrared spectroscopy	FTIR
Scanning electron microscopy	SEM

1.1 Fuel cells

Fuel cell is an electrochemical device in which chemical energy converts directly into electricity. Every fuel cell is made up of three main components: two electrodes, with electrolyte. In general, both the electrodes are mixed conductors i.e. electronic and ionic conductor as well. On the other hand electrolyte should have ionic conductivity which helps in the transfer of ions from cathode to anode and also prevents the mixing of fuel and air. Electricity is produced by REDOX reactions at the electrodes. Fuels (H_2, N_2) are fed at anode and oxygen from air enters at cathode for the completion of electrochemical reaction. One of the great advantages of the fuel cells over other power generating devices such as batteries is that they produce electricity with very little pollution and the byproducts (water & heat) can be further used for various processes.

In general, a single fuel cell produces a very little amount of direct current (DC) electricity (~0.7V). To get a desired amount of power, they can be stacked in series or parallel. Their efficiency is not ruled by the Carnot cycle because no mechanical work is being done in their operation. Batteries work for a limited time, but in case of fuel cells, as long as there is a supply of fuels the process of energy generation continues. There are some limitations of fuel cells, such as the corrosion of its components, instability at high temperatures, etc. [1-5]

1.2 Evolution of fuel cells

Fuel cells have been in existence for nearly one hundred and eighty years. In *1800*, British scientists William Nicholson and Anthony Carlisle explained the process of using electricity to decompose water into H_2 and O_2. Using this approach a German scientist named Christian Friedrich Schoenbein discovered the fuel cell and reported in *1839* that a current is caused by the combination of H_2 and O_2. Simultaneously a Welsh scientist named William Robert Grove was

working on electrolysis and he concluded that it should be possible to reverse the electrolysis process and generate electricity from the reaction of O_2 with H_2. The first fuel cell produced by Grove using platinum electrodes half immersed in sulfuric acid and half enclosed in hydrogen and oxygen is known as 'Grove Cell' or as called by Grove the "gas voltaic battery".

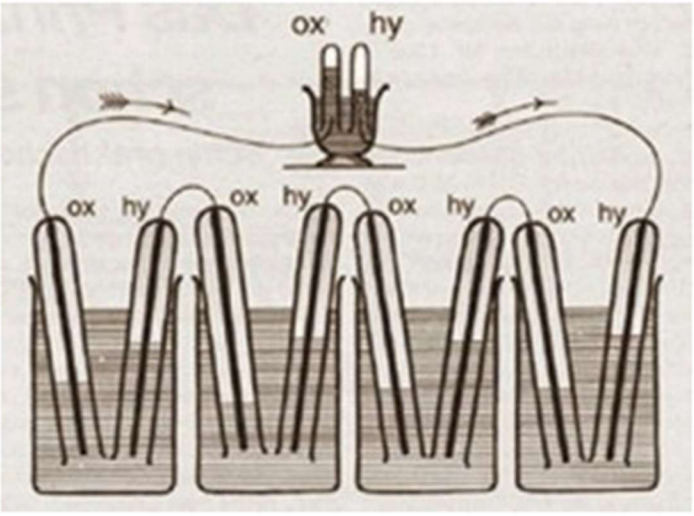

Fig. 1.1: Schematic diagram of Grove Cell. [6]

After about 100 years later, in 1939 British scientist Francis Thomas Bacon modified the original cell by replacing platinum electrodes by nickel gauze and sulfuric acid by non-corrosive potassium hydroxide. This was known as the "Bacon Cell" and it could generate 5kW of energy. Also in *1965*, national aeronautics and space administration (NASA), USA was looking for a way to power the manned space flights and it was at that time the Proton Exchange Membrane Fuel Cell (PEMFC) came into existence and it was successfully used in Gemini-5 space program. In the *1970s* and *1980s* a huge research effort was made to develop the materials for fuel cells and to reduce the cost of this exotic technology. Later, international fuel cells (IFC) developed a 1.5kW alkaline fuel cell (AFC) to use in apollo space missions, which provided electrical power as well as drinking water for astronauts. [6-8]

Fig. 1.2: Power unit used in Gemini-5 space program. [9]

In *1990s,* Japan, Germany and UK government started funding program for the development of PEMFC and solid oxide fuel cell (SOFC) technology for residential micro combined heat and power applications. It was at this time that the direct methanol fuel cell (DMFC) came into picture and these were initially used in soldier-borne power and power for devices such as laptops and mobiles. In mid-*2000s, it* was seen that vehicles using fuel cells provide extended run-time, greater efficiency and simplified refueling framework as compared to their battery equivalent. Various fuel cell buses were introduced in Europe, China and Australia due to their fusion of high efficiency, zero emission of environmental harmful gases and ease of refueling. In late *2000s*, PEMFC using H_2 and natural gas as fuels were used in India and east Africa to provide backup power to mobile phone towers. In recent times we found fuel cells being used in portable, stationary and transport sectors such as in schools, hospitals, banks, etc. and also portable fuel cells are being developed as well. [10-11]

1.3 Types of fuel cells

The name of a fuel cell comes from the type of electrolyte as well as the working temperature of the fuel cells (also depends upon the type of electrolyte being used). The working temperature of

a fuel cell is defined as the temperature at which a sufficiently large number of ions pass from the electrolyte. Fuel cells are classified into five major groups [12-15]:

- Alkali fuel cell (AFC)
- Molten carbonate fuel cell (MCFC)
- Phosphoric acid fuel cell (PAFC)
- Proton exchange membrane fuel cell (PEMFC)
- Solid oxide fuel cell (SOFC)

1.3.1 Alkali fuel cells (AFC)

Compressed H_2 and O_2 are used to produce electricity in AFC. Usually a solution of potassium hydroxide (KOH) in water is used as an electrolyte. The efficiency of this cell is about 70% at an operating temperature of 150 to 200 °C. Its output ranges from 300 watts to 5 kilowatts (kW). Expensive platinum electrodes, pure H_2 fuel and leakage of electrolyte limit its use in power generators. [15]

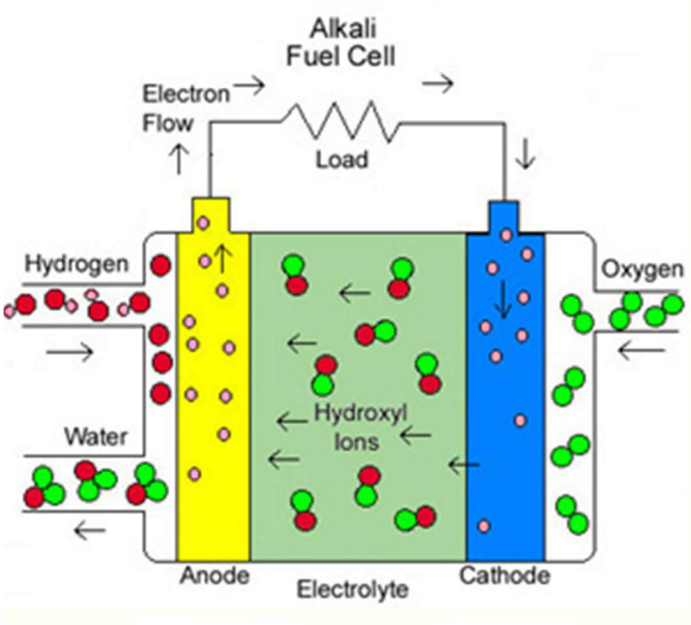

Fig. 1.3: Schematic diagram of an alkali fuel cell. [15]

1.3.2 Molten carbonate fuel cell (MCFC)

High temperature compounds of salt carbonates like magnesium carbonate ($MgCO_3$), sodium carbonate (Na_2CO_3), etc. is used as an electrolyte in this fuel cell. Its efficiency is almost 60% at an operating temperature of 650 °C. Maximum output of molten carbonate fuel cell stack reported till date is 2 MW and designs of units up to 100 MW exists. The poisoning of the cell is limited due to the higher working temperature, but because of the high temperature, their use at home is not preferred. The biggest problem with MCFCs is the emission of carbon dioxide (CO_2) which happens due to the presence of carbonate part in the electrolyte. [16]

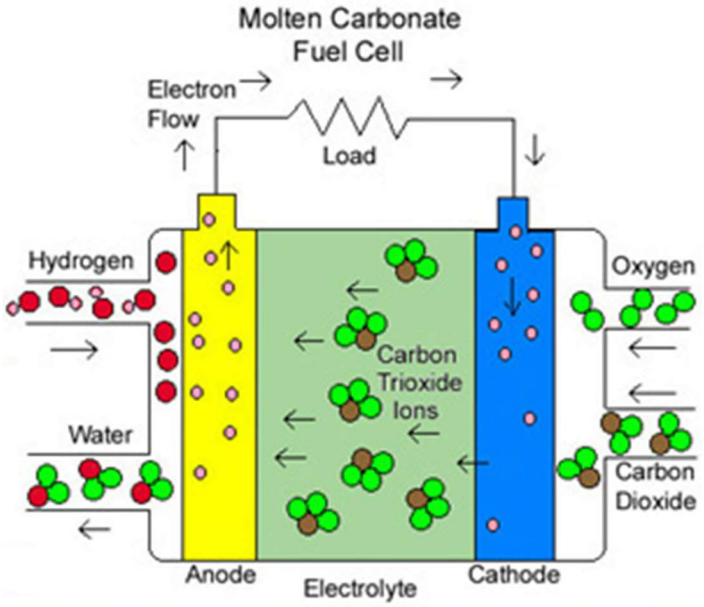

Fig. 1.4: Schematic diagram of a molten carbonate fuel cell. [15]

1.3.3 Phosphoric acid fuel cell (PAFC)

Phosphoric acid is used as an electrolyte in this fuel cell. Its efficiency ranges between 40-55% at an operating temperature (~200 °C). PAFCs have outputs up to 200 kW with an estimated extension of up to 11 MW in the future. The carbon monoxide concentration of about 1.5% is tolerated by this cell broadening the choice of fuels that can be used. In this cell, platinum

electrode-catalysts are needed. Also, its components should be strong enough to sustain in the corrosive acid. [17]

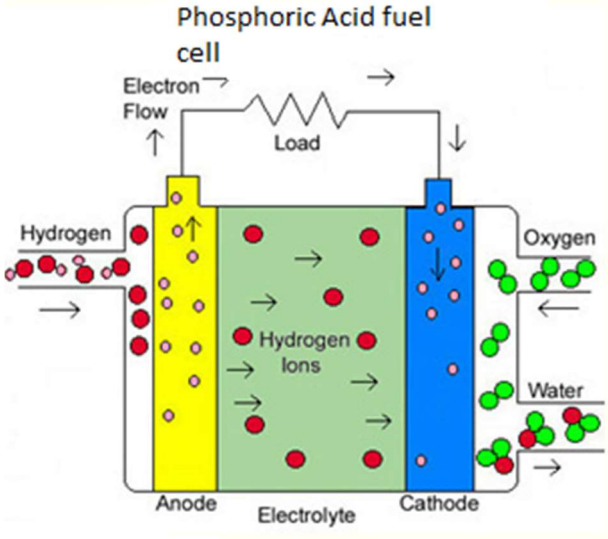

Fig. 1.5: Schematic diagram of a phosphoric acid fuel cell. [15]

1.3.4 Proton exchange membrane fuel cell (PEMFC)

A thin, permeable sheet which is made up of a polymer is used as an electrolyte in PEMFC. Its efficiency is about 40-50% with an operating temperature of ~80 °C. The output of the cell generally ranges from 50 kW to 250 kW. Due to their low operating temperature, these cells can be used in homes and cars. Also, as the electrolyte used is solid and flexible, so there will be no leakage or cracks. [17]

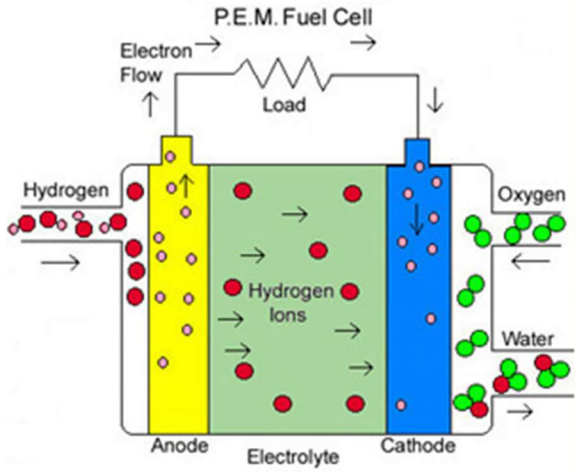

Fig. 1.6: Schematic diagram of a proton exchange membrane fuel cell. [15]

1.3.5 Solid oxide fuel cell (SOFC)

As the name proposes, SOFCs use ceramics as an electrolyte. The maximum reported efficiency of this fuel cell is 75% with operating temperatures ranging from 800-1000 °C. An output of about 100kW can be produced using a single stack of SOFC. No catalyst is required in these fuel cells as the high operating temperature itself is responsible to increase the reaction rate. Among all the fuel cells, solid oxide fuel cells are preferred the most because of the following properties:

1. Higher efficiency
2. Fuel flexibility
3. Negligible pollution
4. Cost effectiveness

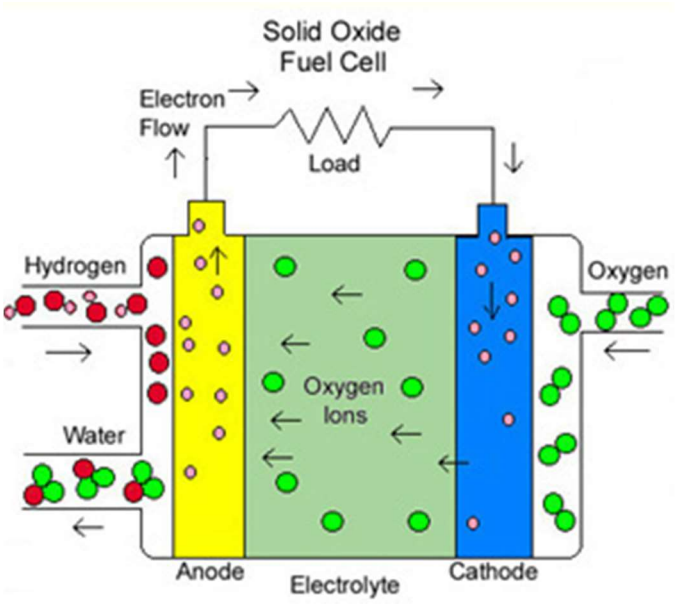

Fig. 1.7: Schematic diagram of a solid oxide fuel cell. [15]

Also these cells require a low amount of maintenance which allows them to be left alone for a long time to produce energy. There are some disadvantages of the higher working temperature which results in electrode sintering, catalyst poisoning, diffusion between electrode and electrolyte materials, and thermal instability, etc. So, nowadays research is being carried out to reduce the

operating temperature of SOFCs. Leading companies in SOFC commercialization are Siemens-Westinghouse (Germany / USA), Sulzer (Switzerland), Global Thermoelectric (Canada), Ceramic Fuel Cells Ltd. (Australia) and Mitsubishi Heavy Industries (Japan). [18-19]

Table 1.1: Different types of fuel cells with their operating temperatures, fuels and efficiencies.

Type	Electrolyte	Operating Temperature	Fuel	Efficiency
Solid oxide fuel cell (SOFC)	Ceramic, solid oxide, zirconia	800-1000°C	Hydrogen or Methane	68-75%
Molten carbonate fuel cell (MCFC)	Molten lithium carbonate	630-650°C	Hydrogen	55-60%
Phosphoric acid fuel cell (PAFC)	Phosphoric acid	190-210°C	Hydrogen	40-45%
Alkaline fuel cell (AFC)	Potassium hydroxide	50-200°C	Hydrogen	50-58%
Proton exchange membrane fuel cell (PEMFC)	Ion exchange membrane	50-90°C	Hydrogen	60%

In table 1.1, the summary of various types of fuel cells with their efficiency are given. The nomenclature of the fuel cells is based on the electrolytes used in them.

1.4 Designs of SOFC

On the basis of their geometry, power density and sealing method, solid oxide fuel cells can be sorted out under two designs:

(a) Tubular Design

(b) Planar Design

1.4.1 Tubular design

Tubular design of SOFC was developed in the *1960s*. In this design the cell is configured as tube and the stack consists of bundles of tubes. Tubular design of SOFCs is preferred because no seals are required in this type cell design. In tubular designs, the tube is built up of cathode material i.e. the cathode supported. The vacuum tube is closed at one ending and electrolyte and anode stuff are formed outside of the tube. [20]

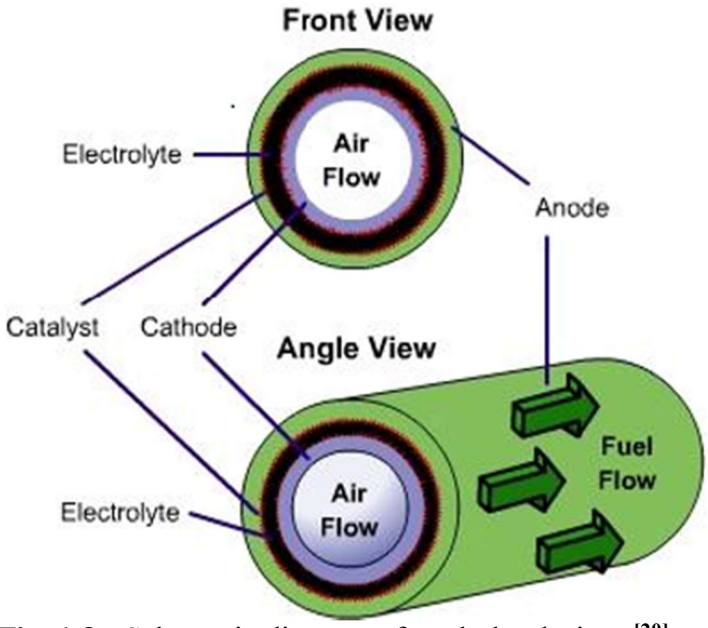

Fig. 1.8: Schematic diagram of a tubular design. [20]

Main features of tubular SOFC are given below:

- No need of sealing in this design
- Performance of the cell is inversely dependent on the diameter of the tube.

1.4.2 Planar design

The planar type design has received much attention recently as it is simpler to construct. The planar type SOFC offers high power density (~ 1MW m^{-3}) as compared to the tubular design which is ascribed to the low electrical resistance due to shorter current paths. Cell components are configured as thin, flat plates.

The planar type SOFC requires high temperature gas seals at the edges of the components. It is designed to have minimum mechanical stress and long term stability. [21]

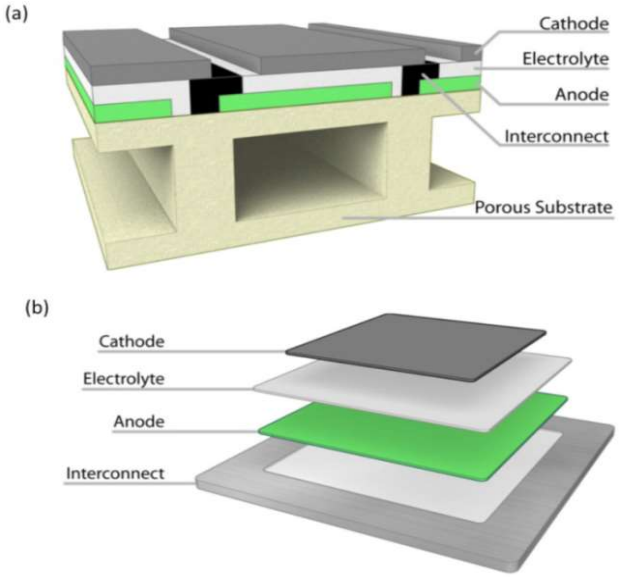

Fig. 1.9: Schematic diagram of a planar design. [21]

1.5 Components of SOFC

The important components used in a solid oxide fuel cell are independent of the type of arrangement of the cell. The representation of traditional components of SOFC is depicted in figure 1.10. Their properties as well as the requirements are as follows:

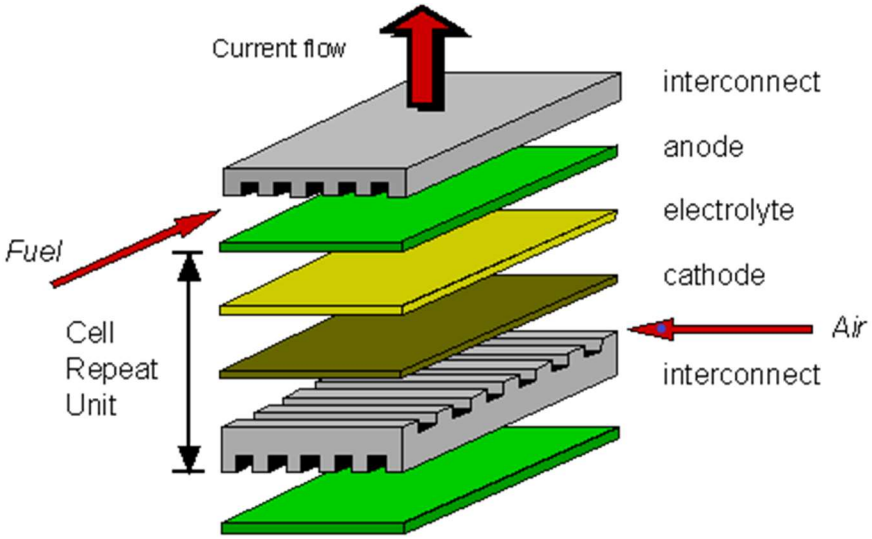

Fig. 1.10: Schematic diagram of components of SOFC. [22]

1.5.1 Anode

Anode is an electrode from where the fuel (H_2, N_2) is fed to the cell. A cermet (ceramic + metal) is used as an anode. Oxidation of fuel takes place at the anode side as:

$$2 \quad O^{2-}(s) + H_2(g) \longrightarrow H_2O(g) + 2e- \qquad \textbf{(1.1)}$$

To get the maximum output from the cell it is preferred to have a large contact line, called as the "Triple Phase Boundary (TPB)". It is the boundary between ionic conductor (ceramic), electronic conductor (metal) and the gaseous phase. The most common cermet used in SOFC's is a mixture of yttria stabilized zirconia (YSZ) and Nickel (Ni). The performance of anode depends on precursor powders used and its microstructure. The degradation is minimum only when the relative size of YSZ particles is smaller than that of Ni.

There are some drawbacks of Ni/YSZ material as it has poor redox stability, Ni can be sintered at the cell working temperature which decreases the porosity of anode, coarsening of nickel when used for long term and deposition of carbon while using hydrocarbons as fuel. Some other anode materials such as Cu-CeO_2-YSZ/SDC, gadolinium doped ceria (GDC), etc. are being used nowadays. [23-24]

1.5.2 Cathode

It is also known as the air electrode, where the reduction of O_2 from air takes place. Air is transported from cathode channel to the TPB and O_2 is reduced according to the following reaction:

$$\tfrac{1}{2}\, O_2(g) + 2e- \longrightarrow O^{2-}(s) \qquad \textbf{(1.2)}$$

A good cathode material should have high electronic conductivity, possesses high porosity for the transportation of O_2 ions from one electrode to the other and should not be oxidized easily under an oxidizing environment. To reduce over potential loses in SOFC's, strontium doped lanthanum manganite (LSM) is used. It was observed that when grain size is decreased to maintain the

porosity, there is an increase in the current density while the over potential loses are reduced. Hence, it can be concluded that multilayer cathodes with smaller grains on inner layers and larger grains on outer layers increase the efficiency of SOFC. Sometimes the reduction of oxygen at cathode limits the performance of SOFC.

1.5.3 Sealant

Thermally stable sealants are required for planar SOFCs along the boundaries of each cell, between stacking of cells and gas manifolds so as to avoid direct combustion of the fuel. Small leaks in seals can reduce the cell performance as well as the cell potential. Therefore, sealants should be airtight during a thermal cycle. Also, sealants should be stable at varying O_2 partial pressures (air and fuel) and chemically well-suited with the components of SOFC. The CTE of the sealants should also be compatible with the other components of SOFC. Usually, alkaline and alkali earth metal containing glass and glass ceramics are used as sealants due to no significant degradation up to 1000 hours of working. The basic problem with sealants is that they can react with all the components of fuel cell during its operation. [25-26]

1.5.4 Interconnect

Several cells are stacked so as to get high output voltage for practical applications. So, SOFC's can be connected in series or parallel with the help of interconnects. Interconnect acts as a bridge for electrical connection between cathode of one cell and anode of other cell. Therefore, it should be a good electrical conductor so as to reduce ohmic losses due to the interconnection of two cells. It prevents the mixing of two gases also preserves the power density of the stack generated. [27-29]

1.5.5 Electrolyte

The electrolyte is one of the most important parts of an SOFC as it helps in maintaining the electrical neutrality of the system. It plays a significant role in the transportation of oxide ions from

cathode to anode via oxygen vacancy hopping mechanism (a thermally activated process) as shown in figure 1.12. Large interionic open spaces which lead to high level of point defect disorder are present in an electrolyte so as to have high ionic conductivity. Generally, in such metal oxides oxygen anion is larger in size than that of the metal cations, so the small cations will have greater mobility in the lattice. [30]

In general, YSZ is widely used as an electrolyte in SOFC's due to high ionic conductivity and better stability under both reducing and oxidizing mediums. [31] Some other examples of solid electrolytes are ZrO_2, CeO_2, Bi_2O_3 based oxides with fluorite structure, $LaGaO_3$ based oxides with perovskite structure, pyrochlores, etc. [31]

1.5.5.1 Properties of good electrolytes

For good performance, an electrolyte is supposed to have open channel crystal structure to provide pathway for easy ionic transportation. An electrolyte should fulfil the following properties: [31]

- It should have less number of transition states.
- It should have fast ionic conduction (0.1 S/cm).
- Their relative density should be high.
- It should be thermodynamically and chemically stable at the operating temperature for sufficiently long duration.
- CTE of electrolyte should match with the other components of SOFC.
- It should possess good mechanical properties.
- It should be chemically inert towards electrode materials.

1.5.5.2 Types of electrolyte materials

There are various materials that can be used as electrolytes for SOFC application. Traditional electrolytes include YSZ, scandia stabilized zirconia (ScSZ) and GDC. The different types of electrolyte materials are:

a) Perovskite-structured oxides

The structure of a perovskite oxide (ABO_3) is shown below. In figure 1.11, red spheres represent the oxygen (O_2) atoms, the blue ones are B-atoms (a small metal cation), and the green sphere gives us the position of A-atom (a bigger metal cation). Oxygen atoms act as a binding agent between A and B.

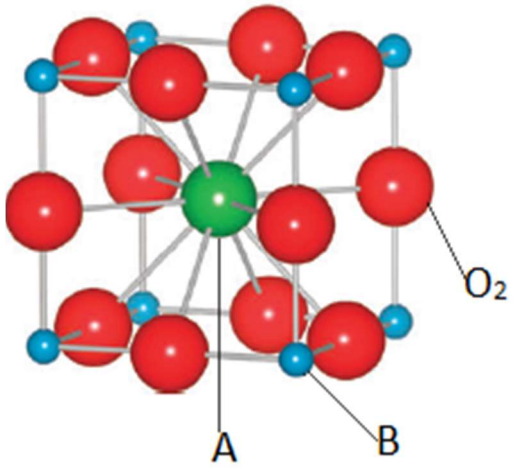

Fig. 1.11: Perovskite structure (ABO_3). [34]

The perovskite materials have very useful properties such as, high thermal power, high ionic conductivity, etc. which make them suitable for making electrolytes.

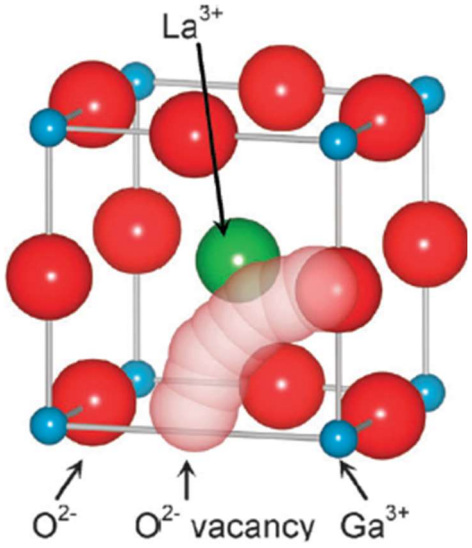

Fig. 1.12: Schematic diagram for oxygen vacancy hopping in $LaGaO_3$. [32]

Perovskite structured oxides doped with Sr (or Mg) such as $La_{1-x}Sr_xGa_{1-y}Mg_yO_{3-\delta}$ (often called as LSGM), show high ionic conductivity over a long range of O_2 partial pressures, with values much higher than that of the conventional electrolytes (such as YSZ, ScSZ, etc.).

b) Fluorite-structured oxides

It is also a good electrolyte materials having formula AO_2, where A is a tetravalent cation. In it the face-center positions are occupied by the cations and the anions occupy the tetrahedral sites between them as shown [34]. Here the oxide ions at different sites have almost similar energies for having high oxide ion conductivity, which makes them a suitable material for SOFC electrolytes. [35]

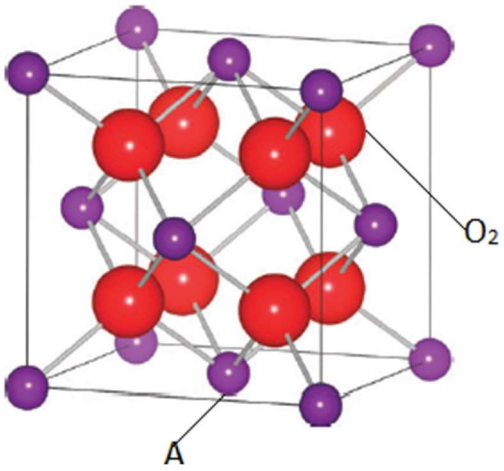

Fig. 1.13: Fluorite structure (AO_2). [34]

c) Aurivillius structured oxides

These are a form of perovskites having general formula (Bi_2O_2) $(A_{n-1}B_nO_{3n+1})$ where A is a large cation having co-ordination number 12, and B is the smaller cation having a co-ordination number 6. These are made by the stacking of $(Bi_2O_2)^{2+}$ and $(A_{n-1}B_nO_{3n+3})^{2-}$ blocks one over the other (n = 1 to 5). It was first observed by B. Aurivillius in 1949 and the advantage of this structure was that it showed ferroelectric behavior even in the simplest form, for e.g. Bi_2WO_6. Later it was observed

that some of the aurivillius type oxides exhibit good oxygen ion conduction such as BIMEVOX (where BI-bismuth, ME-metal, V- V_2O_5, OX- oxygen) and can be used as an electrolyte in SOFCs. [33]

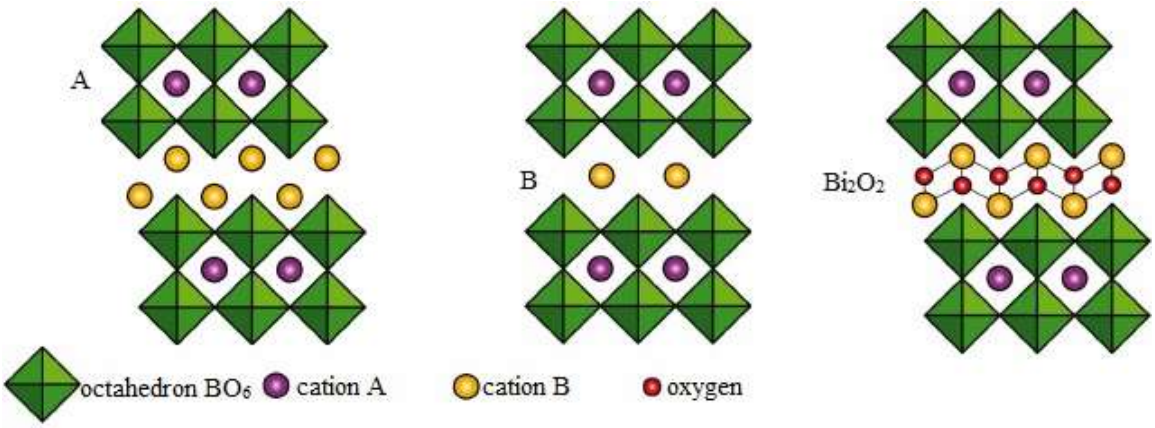

Fig. 1.14: Aurivillius oxide structure. [37]

d) Other electrolyte materials

Some other materials such as $La_2Mo_2O_9$ (LAMOX), BIMEVOX ($Bi_4V_2O_{11}$), can be used as electrolytes other than the traditional ones. These are well known fast oxide-ion conductors. Si and Ge apatites (with general formula $M_{10}(XO_4)_6O_2$), Mayenite ($Ca_{12}Al_{14}O_{33}$), etc. can also be used as electrolyte materials for SOFCs [34]. Bismuth vanadate are also extensively studied by many researchers. It shows good ionic conductivity at 600 °C. However its degradation is fast and grain coarsening also takes place with time. [36]

A lot of research has been carried out to commercialize the fuel cell technology, particularly SOFCs. Major efforts are being made to develop new materials that are having a good ionic conductivity at lower operating temperatures SOFC i.e. at 600-800 °C along with a good chemical stability. For this purpose a lot of materials have been investigated. Nevertheless, these developed materials have their own advantages and disadvantages. In the following chapter, literature review

has been carried out on the electrolytes, particularly for those which can be applied in the intermediate temperature range SOFC.

References:

1. S.A. Boudghene, E. Traversa, Renewable & Sustainable Energy Reviews **6** (2002) 297.
2. B. Ku, Y. Zhang, J. Uni. Sci. Technol. B **15** (2008) 84.
3. V. Kumar, A. Arora, O.P. Pandey, K. Singh, Int. J. Hydrogen Energy **33** (2008) 434.
4. Z. Yang, G. Xia, K.D. Meinhardt, K. Scottwell, J. Stevenson, J. Mater. Eng. Perform. **147** (2005) 107.
5. B.C.H. Steele, A. Heinzel, Nature **414** (2001) 345.
6. A. J. Appleby, J. Power Sources **29** (1990) 11.
7. S.C. Singhal, Solid State Ionics **152-153** (2003) 405.
8. N.Q. Minh, Ceramic fuel cells, J. Am. Ceram. Soc. **76** (1993) 563.
9. www.nasa.gov/feature/gemini-V-paving-the-way-for-long-duration-spaceflight.
10. S.P.S. Badwal, Solid State Ionics **143** (2001) 39.
11. L.J. Gauckler, D. Beckel, B.E. Buergler, E. Jud, U.P. Muecke, Chimia, **58** (2004) 837.
12. J. H. Hirschenhofer, D. B. Stauffer, R. R. Engleman, M. G. Klett, Fuel Cell Handbook, **4th Ed^{n}.** Parsons Corp. USA, 1998.
13. B. C. H. Steele, A. Heinzel, Nature **414** (2001) 345.
14. M.L. Perry, T.F. Fuller, J. Electrochem. Soc. **149** (2002) S59.
15. M. Farooque, H.C. Maru, IEEE Proceedings **89** (2001)1819.
16. W. He, Fuel Processing Technology **53** (1997) 99.
17. R.B. Cervera, Y. Oyama, S. Yamaguchi, Solid State Ionics **178** (2007) 569.
18. S.M. Gheno, V.L. Pimentel, M.R. Morelli, P.I.F. Paulin, Microsc. and Microanal. **19** (2013) 688.
19. A.B. Stambouli, E. Traversa, Renew. Sust. Energ. Rev. **6** (2002) 433.

20. N.Q. Minh, Solid State Ionics **174** (2004) 271.

21. K.S. Howe, G.J. Thompson, K. Kendall, J. Power Sources **196** (2011) 1677.

22. S. Kakac, A. Pramuanjaroenkij, X.Y. Zhou, Int. J. Hydrogen Energy **32** (2007) 761.

23. C. Sun, R. Hui, J. Roller, J. Solid State Electrochem. **14** (2010) 1125.

24. C. Suciu, A.C. Hoffmann, E. Dorolti, R. Tetean, Chem. Eng. J. **140** (2008) 586.

25. J.W. Fergus, J. Power Sources **147** (2005) 46.

26. W.Z. Zhu, S.C. Deevi, Mater. Sci. Eng. A **348** (2003) 227.

27. J.W. Fergus, Mater. Sci. Eng. A **397** (2005) 271.

28. M.L. Faro, D.L. Rosa, V. Antonucci, A.S. Arico, J. Indian Inst. Sci. **84(4)** (2009) 363.

29. J.W. Fergus, Solid State Ionics **171** (2004) 1.

30. A. Taracon, Energies **2(4)** (2009) 1130.

31. N. Mahato, A. Banerjee, A. Gupta, S. Omar, K. Balani, Prog. Mater. Sci. **361** (2015) 7.

32. M. S. Khan, M. S. Islam, D. Bates, J. Phys. Chem. B **102** (1998) 3099.

33. Ismunandara, T. Kamiyamaa, A. Hoshikawaa, Q. Zhouc, B.J. Kennedyc, Y. Kubotad, K. Katoe., J. Solid State Chem. **177** (2004) 4188.

34. L. Malavasi, C.A. J. Fisher, M. Saiful Islam, Chem. Soc. Rev., **39** (2010) 4370.

35. M. Mogensen, D. Lybye, N. Bonanos, P.V. Hendriksen, F.W. Poulsen, Solid State Ionics, **174** (2004) 2.

36. E.D. Bartolomeo, A. D'Epifanio, C. Pugnalini, F. Giannici, A. Longoc, A. Martorana, S. Licoccia, J. Power Sources, **199** (2012) 201.

37. I.A. Rodionov, I.A. Zvereva, Russ. Chem. Rev. **85** (2016) 248.

Various efforts have been made to make suitable electrolyte to achieve desired properties for SOFC application. In the following section research work which has been carried out by various research groups is summarized.

Yahiro *et al.* [1988] studied the ionic conductivity of ceria-samarium based oxide systems with fluorite structure as a function of composition, temperature, partial pressure of O_2 and density. It was observed that the ionic conductivity of $(CeO_2)_{0.80}(SmO_{1.5})_{0.20}$ was ~2 times higher than that of $(CeO_2)_{0.80}(GdO_{1.5})_{0.20}$. As the Sm_2O_3 content increases there is a decrease in the ionic conductivity of the system. Also, with the dopants having radius larger than that of Ce^{4+}, the lattice constant increases and vice versa. [1]

Eguchi *et al.* [1992] investigated the ionic conductivities of ceria-alkaline-earth and rare-earth oxide systems with respect to their structures, and reducibility's. They observed that ceria doped with samarium and gadolinium shows highest electrical conductivities because the radii of Sm^{3+} and Gd^{3+} are comparable to that of Ce^{4+}. On the other hand, the ionic conductivity of $(CeO_2)_{0.8}(SmO_{1.5})_{0.2}$ was observed to be the highest among all the other rare-earth oxide-doped ceria systems. Stability decreases with reduction of ceria and increased electrical conduction even when $(CeO_2)_{0.8}(SmO_{1.5})_{0.2}$ was used as an electrolyte materials. To control this reduction, a thin film of YSZ was deposited which increased the power density of the intermediate temperature SOFC. [2]

Tian *et al.* [2000] examined the ionic conductivities of CeO_2:Y_2O_3 bulk ceramics at different sintering temperatures and concluded that an overall higher DC conductivity was observed while going from higher sintering temperature (1500 °C) to lower sintering temperature (~700 °C). Maximum conductivity was observed at 4-8% doping concentrations of Y_2O_3 whereas the

maximum grain boundary conductivity was found for 10% doping concentration at 1500 °C. It was attributed to lower impurity concentration and lower segregation of the solutes resulting from smaller grain size and large grain boundaries. Overall the highest DC conduction was found for 4% and 0.58% Y_2O_3 doped samples at 1400 °C and 1200 °C respectively. [3]

Lee *et al.* [2005] investigated the electrical conductivity and phase stability of Sc_2O_3 and CeO_2 co-doped with ZrO_2. It can be used as a solid electrolyte material. It shows very good phase stability (cubic phase) during the heating of sample between 1250-1550 °C. However, a very high electrical conductivity was observed for ZrO_2 co-doped with Sc_2O_3 and CeO_2 than YSZ in the temperature range 300-1100 °C. [4]

Zhu *et al.* [2006] developed ceria-based dual phase composites and observed that they have some advantages over the traditional electrolyte materials in SOFCs such as high ionic conductivity and current outputs. It is due to the presence of dual proton and O_2 ion conduction in the composites (ion-doped ceria leads to high oxygen ion conductivity whereas high proton conductivity is due to the salt present). High catalytic activity and proton transportation of these composites increased the overall efficiency of the SOFC. [5] Azad *et al.* [2007] prepared the rare earth doped systems with composition $Ba(Ce, Zr)_{1-x}Sc_xO_{(3-\delta)}$ (x = 0.1, 0.2) using solid state route and found that Sc doping for Ce and Zr was beneficial in increasing the conductivity of the systems (2.58×10^{-4} S/cm to 1.06×10^{-3} S/cm for $x = 0.1$ and 0.2 respectively at 600 °C). [6] Wang *et al.* [2008] synthesized novel core-shell SDC ($Ce_{0.8}Sm_{0.2}O_{1.9}$)/ amorphous Na_2CO_3 nanocomposite having particle size smaller than 100nm for SOFC applications. Ionic conductivity of more than 0.1 S/cm was observed at a temperature of 300 °C, which is applicable for low temperature SOFCs. Power output of 0.8 W/cm^2 was achieved at 550 °C. Moreover, they were found to be suitable for interface and interfacial conduction mechanism. [7]

Ayawanna *et al.* [2009] studied the effects of cobalt on sintering tempertures and ionic conductivities of Sm(Y)-doped ceria solid electrolyte. It was observed that the addition of only 0.5% Co can reduce sintering temperature of both 10 SDC and 2.5Y-SDC samples by ~100 °C. Rapid grain growth along with an improvement of ionic conductivity (almost three fold) was observed when the samples were sintered further at a higher temperature (1400 °C). [8]

Malavasi *et al.* [2010] discussed the structural and mechanistic features of crystalline materials with their ionic properties (including molybdates, gallates, silicate and germanium apatites and niobate systems). It was observed that ionic conduction is a function of flexibility and ease with which the deformation of tetrahedral units takes place. It was also deduced that in Si/Ge apatites the ionic conduction is primarily due to interstitial oxide-ion defects. [9]

Liangdong *et al.* [2011] investigated the microstructure, chemical activity, thermal expansion and electrochemical properties of samaria doped ceria carbonate (SCC). It has showed good compatibility (chemical and thermal) with Ni-based electrodes. The maximum power density gain at 550 °C was 916 $mWcm^{-2}$. With the help of electrochemical impedance spectroscopy it was found that the total ionic conductivity improves, which increases the performance of fuel cell. [10]

Bartolomeo *et al.* [2012] prepared crystalline and homogeneous powders of $BaCe_{0.9-x}NbxY_{0.1O3-x}$ (x = 0.03, 0.06, 0.09 and 0.12) using citrate-nitrate auto combustion process. XRD and X-ray absorption showed that B site of Y-doped barium cerate (BCY) electrolyte was co-doped with Nb^{5+}, which increases the local disorder due to the contraction produced around niobium. BCYN (having the highest Nb content) was the most stable in CO_2. BCYN1 and BCYN2 showed highest conductivities and lowest activation energy in all atmospheres with good sintering behavior in accordance with reduced unit cell volume. $BaCe_{0.84}Nb_{0.06}Y_{0.1}$ was reported as the best electrolyte in terms of chemical stability and proton concentration among all those which were examined. [11]

Singh *et al.* [2012] used citrate-nitrate auto-combustion method to investigate the effect of single doping and co-doping on ionic conductivity enhancement of CeO_2. Radius mismatch and effective index was used to understand the effect of doping. It was deduced from the study that the ionic conductivity was mainly due to diffusion of O^{2-} ions through oxygen vacancies. Single aliovalent doping can be best explained by ionic radius mismatch and effective index. [12]

Arabaci *et al.* [2012] obtained dense CeO_2 ceramics doped with 10 mol% gadolinium ($Gd_{0.1}Ce_{0.9}O_{1.95}$, GDC10) using Pechini method and pellets having relative density of 98% at a temperature of 1400 °C after 6 hours sintering were prepared. The maximum ionic conductivity for the prepared sample was observed to be $3.4x10^{-2}$ S/cm at 500 °C (in air atmosphere). Increased conductivity was assumed to be attributed by high density, small grain size and dopant ion mobility. This showed that GDC10 can be used as an electrolyte material in SOFCs. [13] Suzuki *et al.* [2013] observed the performance of Ni-based anode supported SOFC with doped CeO_2 electrolyte at low temperatures between 294 °C and 542 °C. The maximum power density of the cell was 0.6 W/cm^2 at 542 °C with 47% fuel utilization, and 5 mW/cm^2 at 294 °C. Also, the impedance spectroscopy showed that the influence of gas flow rates on the cell performance was smaller for lower operating temperatures. [14]

Radojkovic *et al.* [2013] studied the chemical stability and electrical properties of the pellets (sintered at 1550 °C) of $BaCe_{0.9-x}Nb_xY_{0.1}O_{3-\delta}$ (BCNY, x = 0.01, 0.03, 0.05, 0.10) doped with Nb using solid state reaction method. This was used as a proton conducting electrolyte for IT-SOFC (between 550-750 °C). Conductivity decreased as the concentration of Nb increases in both wet H_2 and dry Ar atmospheres as well as the highest conductivity was observed for wet hydrogen medium. The conductivity increased with an increasing temperature, in both the mediums. There was an increase in chemical stability with an increase in Nb concentration and the degradation of

BCNY03 and BCNY10 was also prevented due to presence of Nb. [15]

Liu *et al.* [2014] synthesized bismuth and niobium co-substituted $La_2Mo_2O_9$ (LAMOX) by a solid state reaction method. The conductivity values were found to be 0.123 S/cm for x = 0.12, and 0.111 S/cm, for x = 0.2. The thermal stability in highly reducing atmosphere remains good as well as compatible with SOFCs components. [16]

Hou *et al.* [2014] synthesized $Sm_{0.075}Nd_{0.075}Ce_{0.85}O_{2-\delta}Er_{0.4}Bi_{1.6}O_3$ (SNDC|ESB) bilayer structure film by combining one-step co-pressing with drop-coating. The SNDC|ESB structured bilayer film exhibited very good performance among all the reported ceria-bismuth bilayer electrolytes at an operating temperature of ~550 °C. So it can be concluded that the facile fabrication technique provides an effective way to increase the efficiency of low temperature SOFCs performance. [17]

Yu *et al.* [2015] developed $BaCe_{0.8}Y_{0.2}O_{2.9}$-$Ce_{0.85}Sm_{0.15}O_{1.925}$ composite electrolytes using BCY and SDC. The mixing ratio of powders was taken to be 95:5, 85:15, and 75:25 (named as BS95, BS85, and BS75 respectively). It was observed that BS95 and BS85 composites had enhanced ionic conductivities due to composite effect between SDC and BCY phases and no such effect was present in BS75 phase. So, it was concluded that the composite effect decreased with an increase in amount of BCY and vanished after it exceeds a particular limit. Highest conductivity was noticed in the case of BS95 (σ = 0.07808 S/cm) at 800 °C. [18]

Anjaneya *et al.* [2016] studied the lattice parameters, ionic conductivities, activation energies and ionic migration parameters of rare earth ion doped ceria i.e. $Ce_{0.8}Ln_{0.2}O_{2-\delta}$ (Ln = Y^{3+}, Gd^{3+}, Sm^{3+}, Nd^{3+}, and La^{3+}) to be used as electrolyte in intermediate temperature SOFCs. It was observed that Sm doped ceria exhibited highest ionic conductivity (2.36 x 10^{-3} S/cm) followed by Gd, Y, Nd, and La doped samples. The activation energy increased as we go from Sm to La (i.e. Sm < Gd < Y < Nd < La). The change in activation energy followed the Meyer-Neldel compensation rule.

Also the ion migration parameters showed that these samples were ionic in nature which is one of the major requirement for a material to be used as an electrolyte. [19]

Noviyanti *et al*. [2016] synthesized $La_{9.33}Si_6O_{26}$-$Zr_{0.85}Y_{0.15}O_{1.925}$ (LSO-YSZ) using hydrothermal method and made dense pellets by sintering at 1450 °C for 3 hours. Maximum conductivity was observed for the composition LSO-YSZ (7:3), i.e. 1.72 x 10^{-4} Scm^{-1} at 700 °C. Activation energy was observed to be less than 1.1 eV which make these a good material for solid electrolytes. [20]

Xie *et al.* [2017] studied the effect of Nd/Mg co-doping on the electrical properties of CeO_2-based electrolyte materials and reported that an appropriate ratio of Mg to Nd increased the ionic conductivity compared to that in single Nd doping cases. Also the grain-boundary conductivity and total conductivity increased due to the change in oxygen vacancy concentration. [21]

Gao *et al.* [2017] studied the thermal expansion and elastic moduli of yttria stabilized zirconia (YSZ), gadolinia doped ceria (GDC), and scandia and ceria doped zirconia (SCSZ) in the temperature range of 30-900 °C. By using high temperature X-ray diffraction it was observed that the fluorite structure was stable in case of YSZ and GDC whereas a partial phase transformation took place from cubic to rhombohedral and then back to cubic for SCSZ in the temperature range of 300-500 °C. Elastic moduli was found to be highly non-linear for YSZ and SCSZ as they had minimum value of Young's and shear moduli at ~600 °C as well as maximum mechanical loss was observed for SCSZ due to phase transformations. However, in case of GDC the deviation in elastic moduli was observed at very low temperature (200-400 °C) with smaller mechanical losses as compared to doped zirconia ceramics. [22]

References:

1. H. Yahiro, Y. Eguchi, K. Eguchi, H. Arai, J. Appl. Electrochem. **18** (1988) 527.
2. K. Eguchi, T. Setoguchi, T. Inoue, H. Arai, Solid State Ionics **52** (1992) 165.
3. C. Tian, S.W. Chan, Solid State Ionics **134** (2000) 89.
4. D.S. Lee, W.S. Kim, S.H. Choi, J. Kim, H.W. Lee, J.H. Lee, Solid State Ionics **176** (2005) 33.
5. B. Zhu, M.D. Mat, Int. J. Electrochem. Sci. **1** (2006) 383.
6. A.K. Azad, J.T.S. Irvine, Chem. Mater. **21** (2007) 222.
7. X. Wang, Y. Ma, R. Raza, M. Muhammed, B. Zhu, Electrochem. Commun. **10** (2008) 1617.
8. J. Ayawanna, D. Wattanasiriwech, S. Wattanasiriwech, P. Aungkavattana, Solid State Ionics **180** (2009) 1394.
9. L. Malavasi, C.A.J. Fisher and M.S. Islam, Chem. Soc. Rev. **39** (2010) 4370.
10. L. Fan, C. Wang, M. Chen, Jing Di, J. Zheng, B. Zhu, Int. J. Hydrogen Energy **36** (2011) 9987.
11. E.D. Bartolomeo, A. D'Epifanio, C. Pugnalini, F. Giannici, A. Longoc, A. Martorana, S. Licoccia, J. Power Sources **199** (2012) 201.
12. N.K. Singh, P. Singh, D. Kumar, O. Parkash, Ionics **18** (2012) 127.
13. A. Arabaci, M.F. Oksuzomer, Ceram. Int. **38** (2012) 6509.
14. T. Suzuki, B. Liang, T. Yamaguchi, H. Sumi, K. Hamamoto, and Y. Fujishiro, Int. J. Appl. Ceram. Technol. **12** (2013) 5.
15. A. Radojkovic, M. Zunic, S.M. Savic, G. Brankovic, Z. Brankovic, Ceram. Int. **39** (2013) 307.

16. X. Liu, H. Fan, J. Shi, G. Dong, Q. Li, Int. J. Hydrogen Energy **39** (2014) 17827.

17. J. Hou, L. Bi, J. Qian, Z. Zhu, J. Zhang, W. Liu, J. Mater. Chem. A **00** (2014) 1.

18. J. Yu, N. Tian, Y. Deng, G. Li, L. Liu, L. Cheng, P. Gao, Q. Pan, Y . Wang, X. Chen, K. Qi, Science China Chemistry **58** (2015) 3.

19. K.C. Anjaneya, J. Manjanna, V.M.A. Kumar, H.S. Jayanna, C.S. Naveen, Adv. Mater. Lett. **7(9)** (2016) 743.

20. A.R. Noviyanti, F.S. Irwansyah, S. Hidayat, A. Hardian, D.G. Syarif, Y.B. Yuliyati, I. Hastiawan, AIP Conf. Proc. **1712** (2016).

21. S. Xie, Y. Liu, W. Xi, D. Zhou, J. Meng, Mater. Res. Innovations **2** (2017) 1433.

22. P. Gao, A. Bolon, M. Taneja, Z. Xie, N. Orlovskaya, M. Radovic, Solid State Ionics **300** (2017) 1.

This chapter presents the details of sample processing and characterization techniques which were followed during the course of present study.

3.1 Sample preparation:

Samples were prepared by the mixing of raw materials CeO_2 and Na_2O with purity ≥ 99% from LOBA Chemie, India in an agate mortar followed by the conventional solid state reaction method. Every batch contained a suitable mole fraction of preferred initial ingredients. The sample compositions with their respective labels (ID) are given in table 3.1:

Table 3.1: sample composition (mol %) with their labels (ID).

Sample ID	CeO_2	Na_2O
CNH-5	95	5
CNH-10	90	10
CNH-15	85	15
CNH-20	80	20

For every system, raw materials were taken as per the required stoichiometric ratio. The mixture was grounded to break the clustered particles. The ground powder was moved to a re-crystallized alumina crucible and put in a high temperature furnace. Initially, the samples were heated at 1250 °C for 2 hours to facilitate the calcination process. Moisture is released during the calcination. After this the obtained powder was again grounded so as to break the coagulation of particles. This grounded powder was used to make pellets of dimensions 10 mm x 8 mm x 4 mm under the load of 12kN/ cm^2. In the next step these pellets were sintered at 1300 °C for 12 hours in the high temperature furnace. The sample preparation details along with relevant information about the performed characterizations are given in the flow chart as presented in Fig. 3.1.

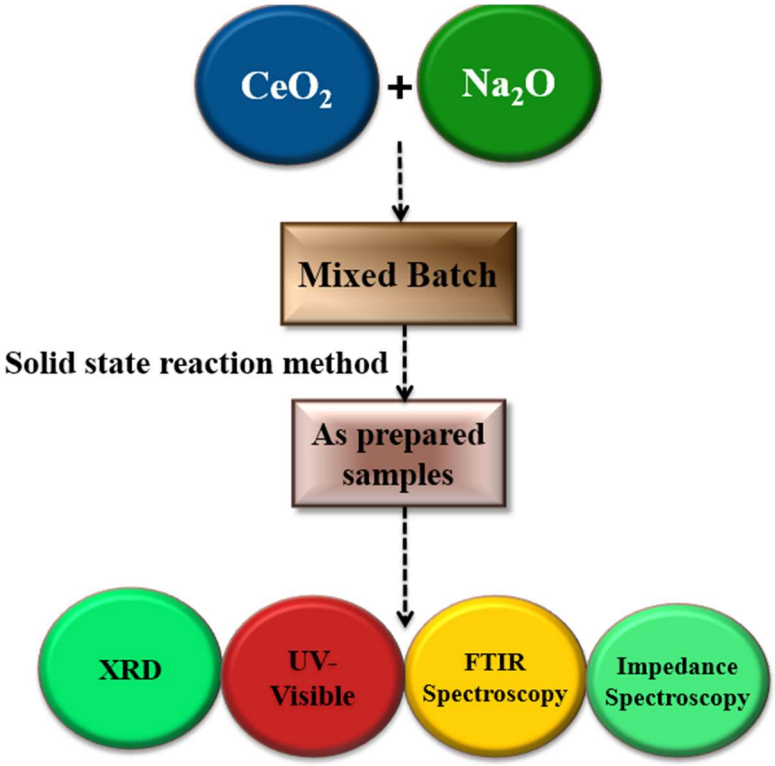

Fig. 3.1: Flow chart showing path chosen for sample preparation and characterization of prepared samples.

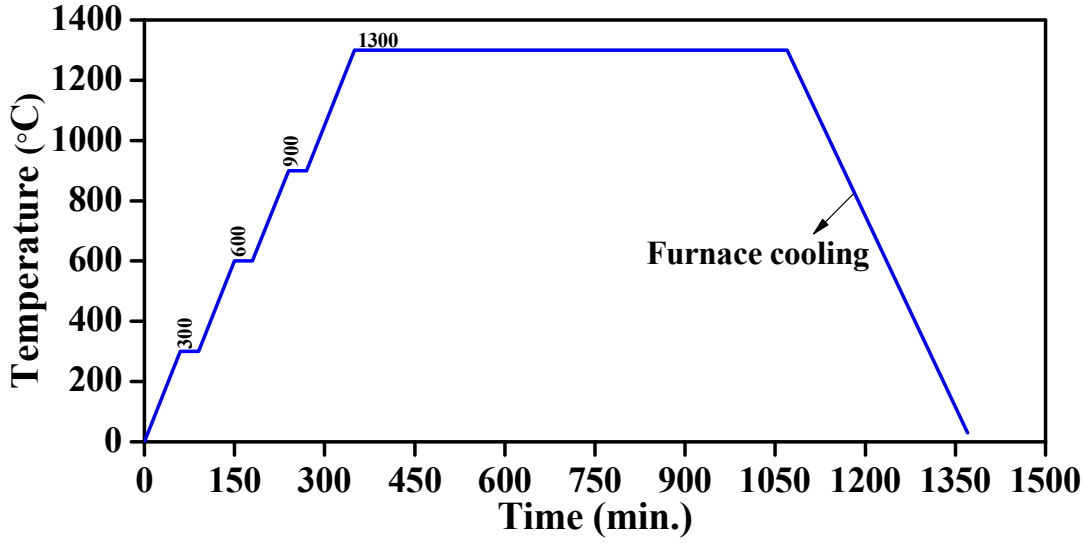

Fig. 3.2: Program followed for sintering of the compositions.

The program followed for the calcination and sintering in the high temperature furnace at 1250 °C and 1350 °C respectively, are shown in figure 3.2.

3.2 Characterizations:

The as-prepared samples were characterized using different techniques so as to check their appropriateness as electrolyte for SOFC's. Structural aspects of the as-prepared samples were observed by the use of the X-ray diffraction technique. The CTE was measured using dilatometry to check the compatibility of our samples with other parts of the SOFC. UV-Visible spectroscopy was used to analyze the optical properties of the prepared samples. The particulars of these techniques are as follows:

3.2.1 Density measurement

The density of the as-prepared samples was measured using Archimedes principle with xylene as immersion medium:

$$\rho_{sample} = \frac{W_a}{W_a - W_b} (\rho_{xylene}) \quad \textbf{(3.1)}$$

where, ρ_{sample} is the density of the sample, ρ_{xylene} is the density of xylene, W_a is the weight of the sample in the air and W_b is the weight of the sample in xylene. The density of xylene at room temperature is 0.863 g/cm^3. This density was used to calculate the molar volume (V_m) of the as-prepared samples using the following relation:

$$V_m = \frac{M}{\rho} \quad \textbf{(3.2)}$$

3.2.2 X-ray diffraction (XRD)

Structural properties of a crystalline/amorphous material can be primarily analyzed by using XRD. XRD is used to calculate crystallite size, volume fraction, crystallite size and the disordering in the sample. The material should be ground in good manner to determine its average bulk composition.

It is a non-destructive method which helps us in the phase identification of the material, provides information about the unit cell dimensions and volume fractions of the crystalline materials. The

incidence and reflection phenomenon of X-rays by the atomic planes of the sample is shown below:

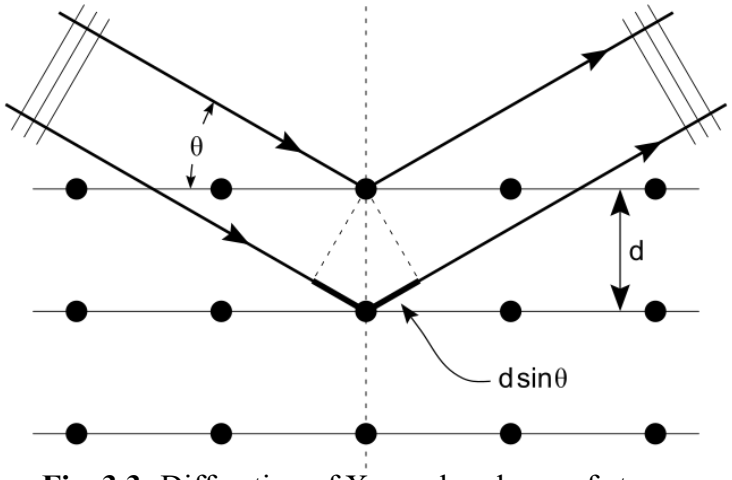

Fig. 3.3: Diffraction of X-rays by planes of atoms.

In XRD, monochromatic X-rays are incident on the sample and the reflected part is recorded by the counters (as shown in figure 3.4). In the present study, XRD patterns at room temperature were recorded using PANalytical X'perts PRO MPD Diffractometer with Cu Kα radiation (λ = 1.54 Å) obtained from a copper target using a built-in Ni filter. The 2θ values of the XRD pattern were taken in the range of 10-85° (degree) at the scan rate of 5°/min.

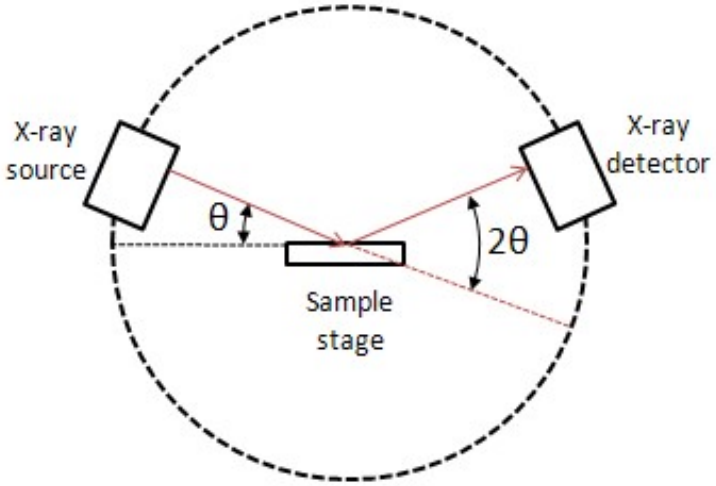

Fig. 3.4: Schematic representation of the principle of XRD.

Constructive interference along with a diffracted ray is observed when the incident rays interact with the samples and when the Bragg's law is satisfied, which is given as:

$$n\lambda = 2d\sin\theta \tag{3.3}$$

where n, λ, and d are positive integer, wavelength of the incident wave and distance between the planes, respectively.

3.2.3 Fourier transform infrared (FTIR) spectroscopy

FTIR Spectroscopy is an analytical technique used to identify "organic, polymeric, and in inorganic materials". This technique uses infrared light to scan the test samples and observe the chemical functional groups present in it. Gases, solids, and liquids can all be analyzed with the help of IR spectroscopy. The spectrum of an unknown material can be identified by comparison with known compounds. A schematic layout of FTIR spectrometer is shown in figure 3.5. IR absorption information is represented as a spectrum between wave number on the x-axis and absorption intensity/percentage transmittance on the y-axis.

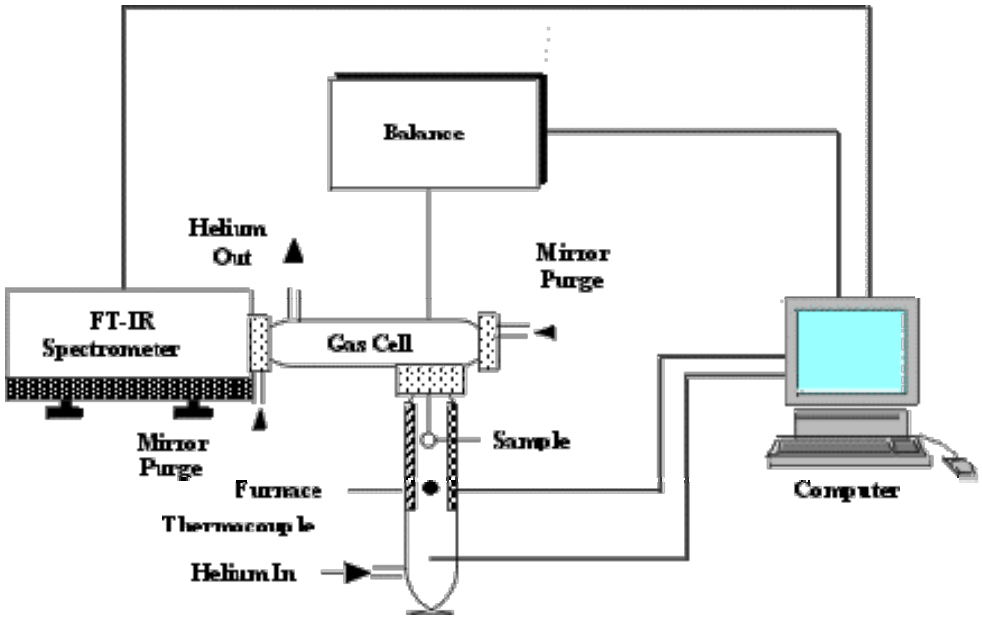

Fig. 3.5: Schematic representation of FTIR.

3.2.4 UV-Visible spectroscopy

Various wavelengths of light are absorbed by a material in and near the visible region. UV-Visible spectroscopy involves the measurement of this light absorption by the material in the visible region and adjacent regions of ultraviolet (UV) and infrared (IR) ranges. Here the molecules undergo a transition from ground state to excited state and then back to the ground level. A UV-Visible spectrometer is shown in figure 3.6:

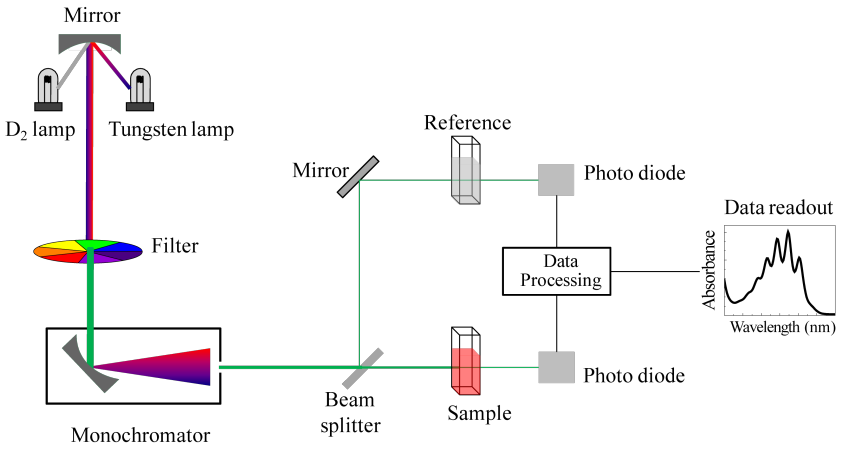

Fig. 3.6: Schematic of UV-Visible spectrometer.

This technique helps us in the measurement of emission, absorption, and transmission of ultraviolet and visible wavelength by the atoms of the material. In the present study, the optical transmission spectra of the as-prepared samples were recorded at room temperature using Perkin Elmer 55 UV-Visible spectrometer in the wavelength range of 200-800 nm. Energy band gap of the as-prepared samples was calculated by the obtained data.

3.2.5 Scanning electron microscopy (SEM)

SEM is used to produce images of a sample with the help of a focused electron beam. The atoms of the sample interact with this beam of electrons and various signals are produced which contain information about the topography and composition of the sample. Commonly, the secondary electrons produced by the electron beam are detected and an image displaying the tilt of the sample

surface is generated. SEM micrographs have a have a large field depth which is due to the narrow electron beam used and this helps us in understanding the surface of the sample with more precision.

In this chapter the results and discussion is presented for the as synthesized samples. The samples are prepared by solid state reaction method.

4.1 Density and molar volume analysis

The calculated values of densities, relative densities, and molar volume of the as-prepared samples are listed in Table 4.1. The densities of all the as-prepared samples is calculated using Archimedes principle. The molar volume is also calculated using following equation:

$$V_m = \frac{M}{\rho} \quad \textbf{(4.1)}$$

where, M and ρ are the molar weight and density of the as-prepared samples, respectively.

Table 4.1: Densities, molar volume and relative densities of as-prepared samples.

Sample ID	Density (ρ) (g/cc)	Theoretical density (g/cc)	Relative density	Molar volume (V_m) (cc/mole)
CNH-0.05	6.89	7.32	94.14	23.93
CNH-0.10	6.68	6.99	95.52	23.63
CNH-0.15	6.66	6.75	98.76	22.64
CNH-0.20	6.62	6.68	99.11	21.70

The density of the samples decreases as the concentration of Na_2O increases in CeO_2. This is because CeO_2 is heavier than that of Na_2O. Therefore, the observed trend is in association with the replacement of denser CeO_2 (7.65 g/cm^3) with lighter Na_2O (2.27 g/cm^3). The as-prepared samples exhibit more than 90% relative density. It means that the addition of Na_2O increase the sinterability of CeO_2. In general ceramic materials exhibit poor sinterability and higher porosity [1]. CNH-0.05 shows highest molar volume as compared to other samples. The minimum molar volume is observed for CNH-0.20 sample. Figure 4.1 gives the relation between density and molar volume of the as-prepared samples with increasing doping concentration of Na_2O.

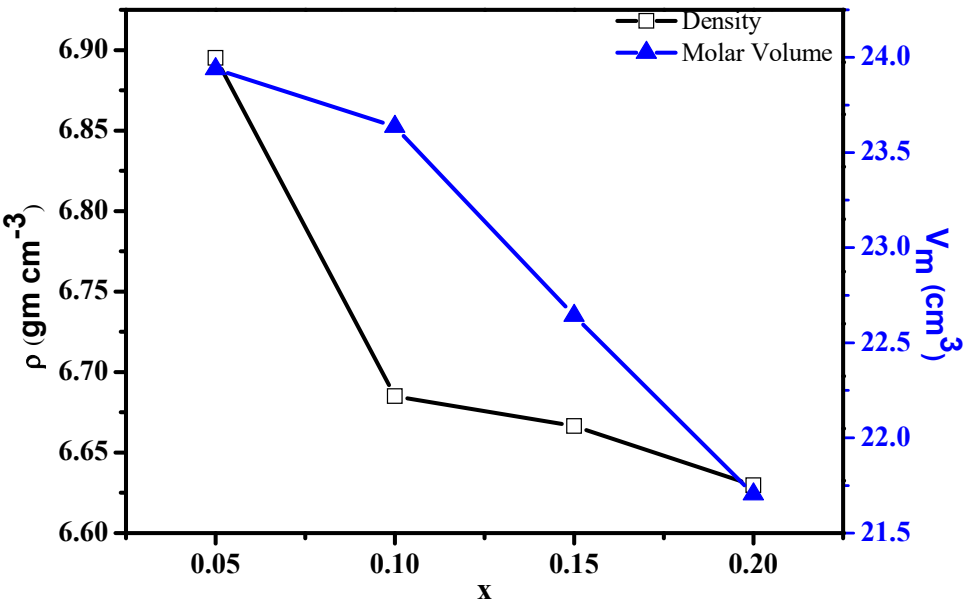

Fig. 4.1: Density vs. molar volume plot for $Ce_{1-x}Na_xO_{2-\delta}$.

4.2 X-ray diffraction (XRD) analysis

XRD patterns of all the as-prepared samples are shown in figure 4.2. It clearly indicates that all the samples are crystalline in nature, as sharp peaks are observed in the XRD patterns of all the samples.

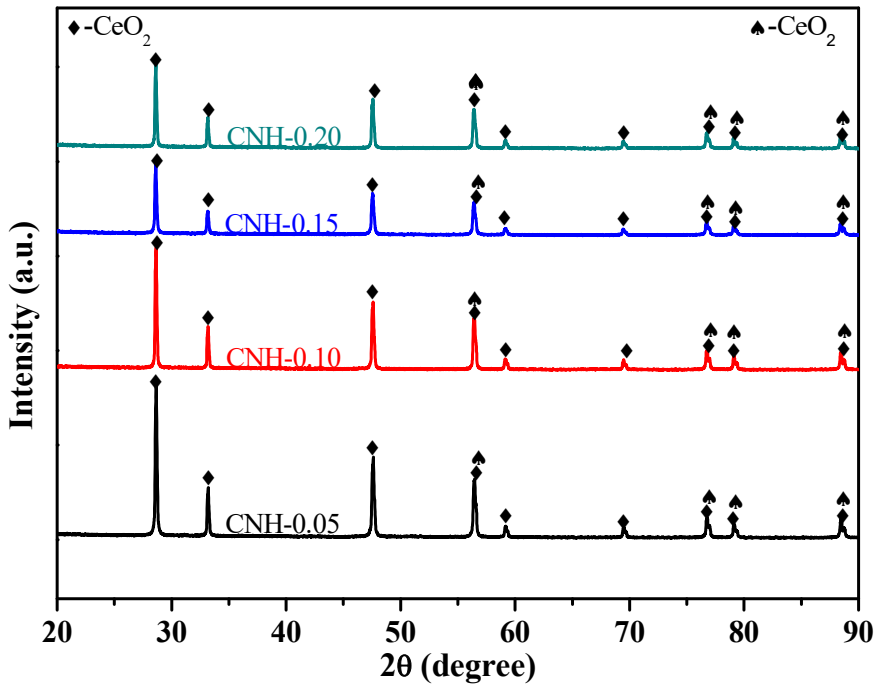

Fig. 4.2: XRD patterns of all the as-prepared samples.

Table 4.2: Lattice parameters of all the as-prepared samples for CeO_2 (ICDD card no. 03-065-5923).

	CNH-0.05	**CNH-0.10**	**CNH-0.15**	**CNH-0.20**
a (Å)	5.394	5.397	5.401	5.400
b (Å)	5.394	5.397	5.401	5.400
c (Å)	5.394	5.397	5.401	5.400

The present samples contain two crystalline phases of CeO_2 with two different ICDD card no. as 03-065-5923 and 00-034-0394, respectively. The volume fraction of the crystalline phases are calculated by direct comparison method [13]. Also, both the XRD peaks are slightly different to each other.to estimate the presence of both the phases, refinement of XRD data is required.

The lattice parameters of all the samples are given in Table 4.2. It can be seen that the contribution in volume fraction of samples is more for ICDD card no. 03-065-5923 than card no. 00-03-0394 i.e. ~ 56% and 44%, respectively. In addition to this, the intensity of the XRD peaks decreases with increasing concentration of Na_2O (from CNH-0.05 to CNH-0.20) which can be due to some disordering which has taken place with Na_2O doping in the CeO_2 phase.

4.3 FTIR analysis

FTIR spectra of all the as-prepared samples are recorded in the region 4000-400 cm^{-1} at room temperature. The FTIR spectra of all the samples are shown in figure 4.3. The major IR bands are observed around 1630 cm^{-1}, 1435 cm^{-1}, 1062 cm^{-1}, 830 cm^{-1}, 720 cm^{-1} and 500 cm^{-1} with a change in band intensities and minor change in peak positions with respect to each other. The broad band, corresponding to the Ce-O stretching mode of CeO_2 is seen at 510 cm^{-1} [2]. The small bands at 723 cm^{-1} and 836 cm-^{1} are assigned to symmetric stretching of the bridging oxygen and (Ce-O) metal-oxygen bond, respectively.

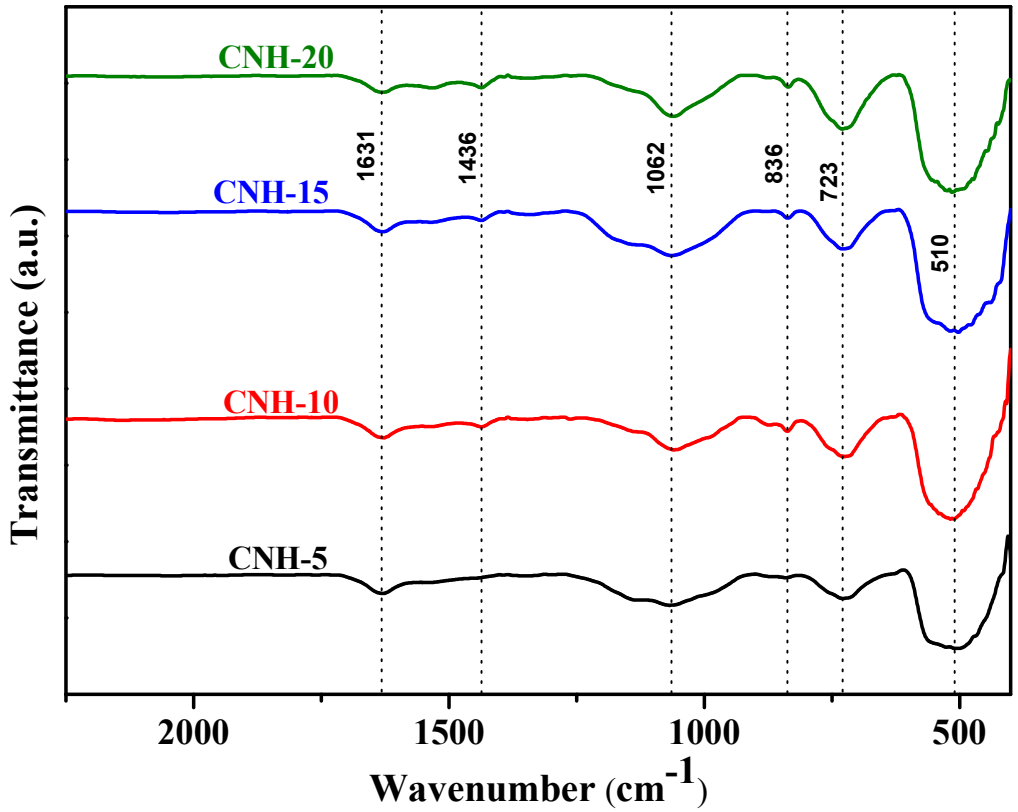

Fig. 4.3: FTIR spectra of all the as-prepared samples.

Other broad band is observed at 1062cm^{-1} which corresponds to commercial CeO_2 powders [3]. The band observed at 1436 cm^{-1} is not indexed. However, it may be generated due to the Ce-O-Na bond due the bands of Ce-O and Na-O. So, probably this band is associated with the combination of dopant and host. The absorption band at 1630 cm^{-1} shows physically absorbed water molecules [4]. The assignment of bands of the FT-IR spectra of all the as-prepared samples have been given in accordance to reported data in literature.

4.4 UV-Visible spectroscopy analysis

The diffused reflectance spectra of all the as-prepared samples are shown in figure 4.4. The highest value of reflectance for all the samples is observed at ~ 700 nm whereas the lowest value is observed at a wavelength of ~ 365 nm. From this diffused reflectance spectra, the optical band

gaps of all the as-prepared samples are calculated by using Kubelka-Munk function which is given as:

$$F(r) = \frac{(1-r)^2}{2r} \quad \textbf{(4.2)}$$

where, F(r), and 'r' are the Kubelka-Munk function, and reflectance, respectively. To calculate the optical band gap of the as-prepared samples, (F(r)hυ) vs. hυ plots are extrapolated to meet the hυ corresponding to $(F(r)h\upsilon)^2 = 0$ as shown in figure 4.5. The intercept of this extrapolation on energy axis gives us the optical band gap value of samples [5].

The optical band gap values for all the as-prepared samples are in the insulating range as seen in table 4.3. Urbach energy (E_U) of the as- prepared samples is measured by the equation $\alpha(\upsilon) = \beta \exp(h\upsilon/E_U)$. The reciprocal of the slope of linear portion from (F(r) vs. hυ plot gives us the urbach energy of the samples [6].

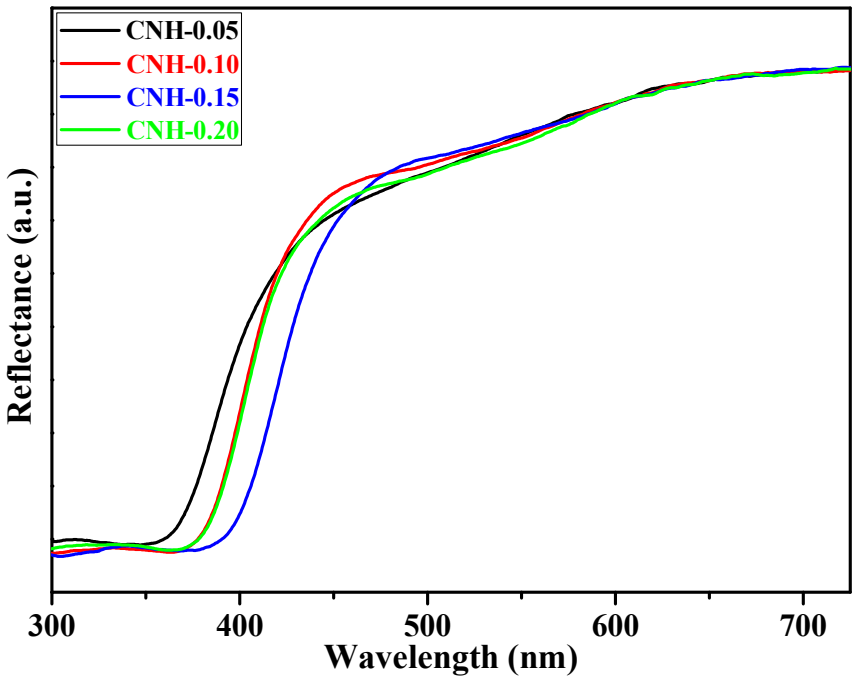

Fig. 4.4: Diffused reflectance spectra of all the as-prepared samples.

CNH-0.05 sample have the highest optical band gap (3.21 eV) and the band gap decreases as the content of Na_2O increases from CNH-0.05 to CNH-0.15 except for CNH-0.20. This can be attributed to the fact that CNH-0.05 possess the lowest Na_2O concentration.

Table 4.3: Optical band gap and urbach energy of all the as-prepared samples.

Sample ID	**CNH-0.05**	**CNH-0.10**	**CNH-0.15**	**CNH-0.20**
Optical band gap (eV)	3.21	3.12	3.03	3.07
Urbach energy	0.161	0.161	0.147	0.160

Generally, optical band gap decreases due to impurities and defects created by the dopants. Sometimes the energy levels lies between conduction and valence band of the host materials. The urbach energy could not show any trend in the present samples.

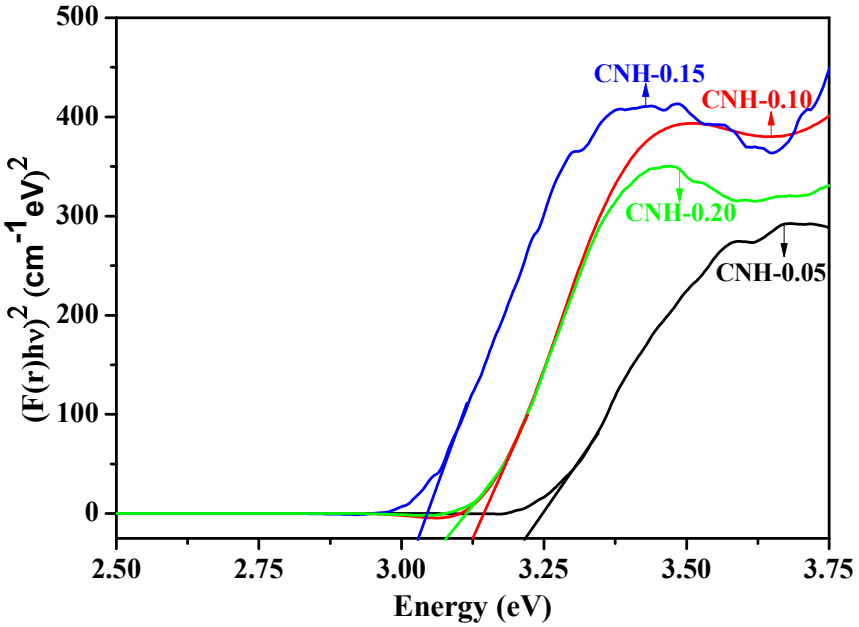

Fig. 4.5: Band gaps of all the as-prepared samples.

4.5 SEM analysis

The representative SEM micrographs along with their particle size distribution curves of the fractured surface of the CNH-0.10 and CNH-0.20 samples are shown in figure 4.6 and figure 4.7,

respectively. The SEM micrographs pronounce that the morphology of the two systems is non uniform as both distorted spherical and faceted geometry (marked as yellow rings) of the particles is observed as well as the particles are agglomerated in the samples which may be the reason behind high relative density of the present samples.

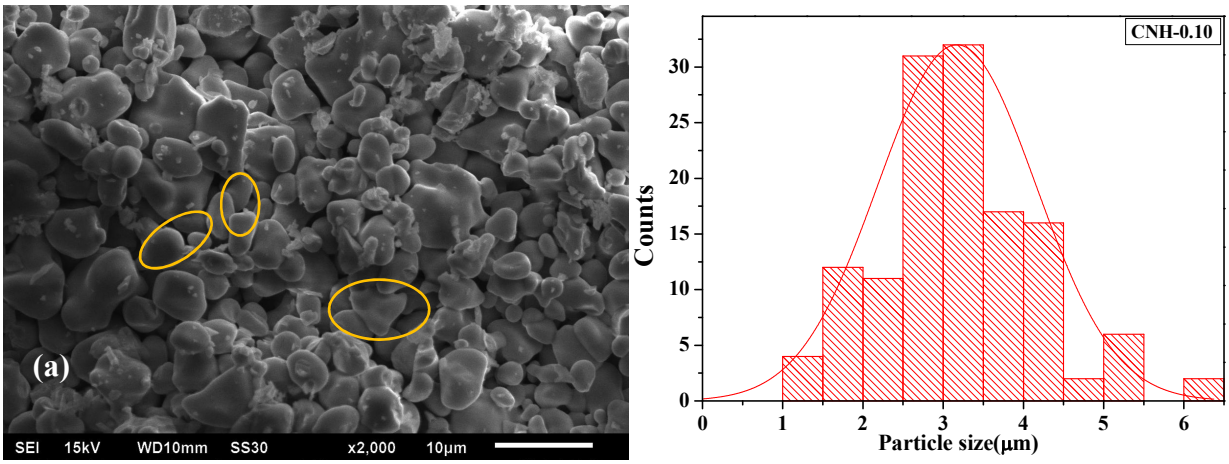

Fig. 4.6: SEM photograph and particle size distribution curve of CNH-0.10.

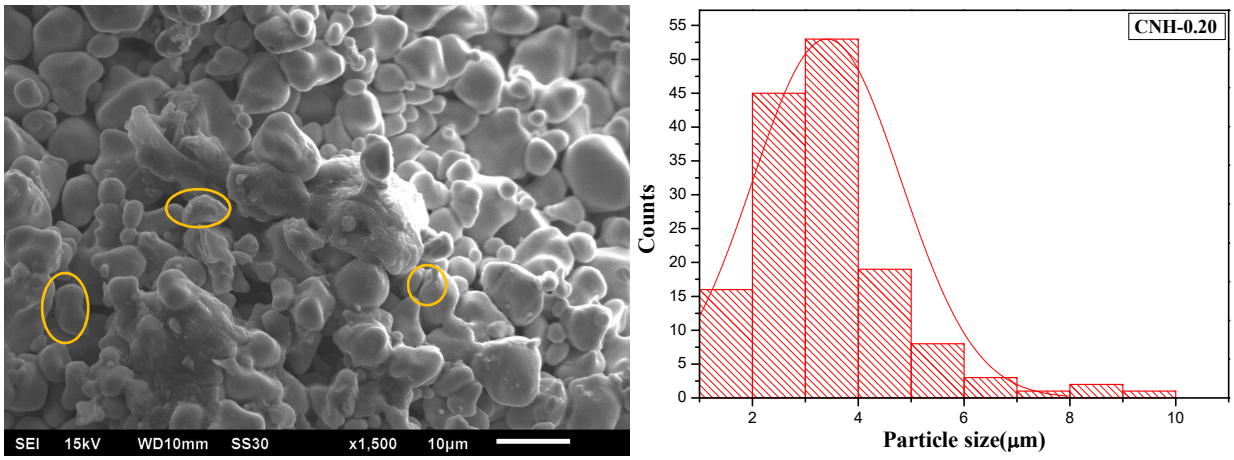

Fig. 4.7: SEM photograph and particle size distribution curve of CNH-0.20.

As observed from the normalized particle distribution curves, the particle size distribution is wide and the average size of the particles in CNH-0.10 is ~3.15µm whereas in the case of CNH-0.20 it is observed to be ~3.5µm.

4.6 Conductivity measurement

The Au coated samples were characterized for ac conductivity with frequency and temperature. No semicircle was observed below 350 °C. After this temperature (350 °C), the complete semicircles are observed for all the as-prepared samples. The maximum and minimum radius of the semi-circle is observed for CNH-0.10 and CNH-0.05 samples, respectively as shown in figure 4.8. For the variation of conductivity with temperature, the representative Arrhenius plots (between ln(σT) and 1000/T) for CNH-15 and CNH-20 are shown in figure 4.9. [7, 8] The conductivity for all the samples is calculated using the following relation;

$$\sigma = l/RA \qquad \textbf{(4.3)}$$

Where, l is thickness, A is cross-sectional area of Au coated pellets and R is the resistance of as-prepared samples. It is calculated from the point of intersection of Cole-Cole semicircle plot on the X-axis. The conductivity curves show a deviation around 600 °C which may be attributed to the phase transition [9].

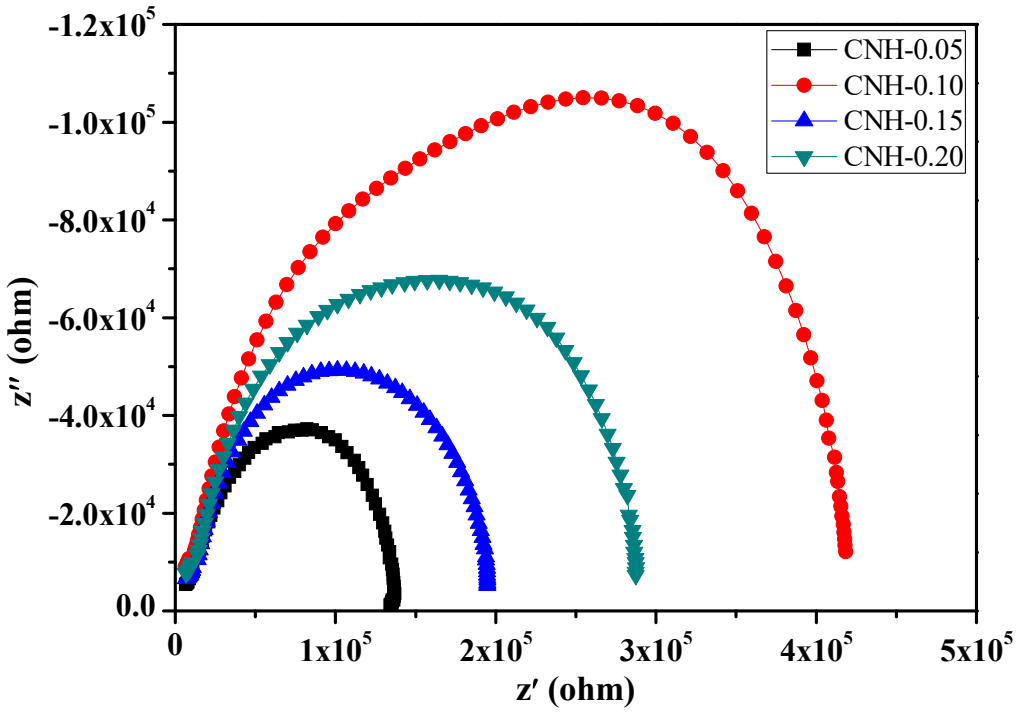

Fig. 4.8: Cole-cole plots of all the as-prepared samples.

The activation energy of the as-prepared samples is calculated using the relation:

$$\sigma T = \sigma_0 \, exp\left(\frac{-E_a}{kT}\right) \quad \textbf{(4.4)}$$

Where σ_0 is pre-exponential factor, E_a is activation energy for conduction, k is Boltzmann constant and T is the absolute temperature. The activation energies are listed in the table 4.4. The conductivity is mainly due to polaron conduction mechanism at low temperature on the other hand, at higher temperature it can be related to oxygen vacancies leading to high ionic conductivity. So change in slope can be due to change in number of charge carriers with temperature.

In general, conductivity increases with an increase in the doping concentration but in the present study, the conductivity decreases, which can be associated to defect association and clustering with an increase in the doping amount in CeO_2. Also, with an increase in doping concentration there is an increase in oxygen vacancies and maybe the ordering of oxygen vacancies could have taken place which leads to a decrease in the conductivity. [10]

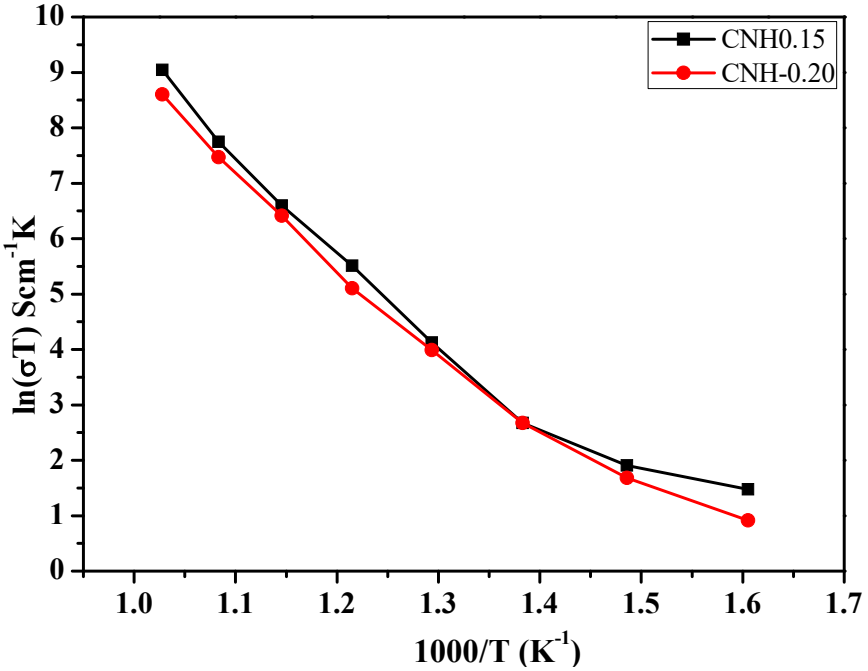

Fig. 4.9: Arrhenius curves of CNH-0.15 and CNH-0.20 samples.

In addition to this, the maximum conductivity (12 x 10^{-7} Scm^{-1}) is observed for CNH-0.05 sample at 700 °C as shown in table 4.3 which is due to the higher density (6.89 g/cc) of this sample as compared to the other samples. [11] Also, as the volume fraction increases the grain size decreases which further leads to an increase in grain boundaries. The increase in grain boundaries leads to an increase in the conductivity because the hopping mechanism takes place easily. So, the maximum conductivity observed for CNH-0.05 may be due to the high volume fraction of CeO_2 (ICDD card no. 00-03-0394) as discussed in section 4.2 [14]. However, the order of conductivity is not changed with the dopant concentration. The maximum and minimum values of activation energy are observed for CNH-0.20 and CNH-0.05, respectively between temperatures 600 °C - 700 °C. The conductivity value is lower than the reported value even for the pure CeO_2 sample [12]. The doping of Na_2O in CeO_2 is not beneficial in the present samples to enhance the ionic conductivity of the system.

Table 4.4: Activation energy and conductivity of all the as-prepared samples.

Sample ID	**Activation energy, E_a (eV)**		**Conductivity, σ (x10^{-7} S/cm)**
	350°C< T < 600°C	**600°C<T<700°C**	**At T=700 °C**
CNH-0.05	1.76	.21	12
CNH-0.10	.94	.23	3.12
CNH-0.15	1.51	.46	8.7
CNH-0.20	1.43	.67	5.6

References:

1. I. Riess, D. Braunshtein, and D.S. Tannhauser, J. Am. Ceram. Soc. **64** (1981) 8.
2. M. Farahmandjou, M. Zarinkamar, J. Ultraf. Gra. Nanostr. Mater. **48** (2015) 5.
3. E. Kumara, P. Selvarajanb, D. Muthurajc, Materials Research **16** (2013) 269.
4. K.K. Babitha, A. Sreedevi, K.P. Priyanka, B. Sabu, T. Varghese, Indian J. Pure Appl. Phys. **53** (2015) 596.
5. A.E. Morales, E.S. Mora, U. Pal, Rev. Mex. Fis **53** (2007) 18.
6. R.K. Waring Jr., W.Y. Hsu, J. Appl. Phys. **54** (1983) 4093.
7. X.L. Xia, Z.G. Liu, J.H. Ouyang, Solid State Ionics **196** (2011) 1840.
8. S. Thakur, O.P. Pandey, K. Singh, Ceram.Int. **39** (2013) 6165.
9. C.K. Lee, A.R. West, Solid State Ionics **86** (1996) 235.
10. S. Yilmaz, O.Turkoglu, M.Ari, I.Belenli, Ceramica **57** (2011) 185.
11. F. Krok, W. Bogusz, P. Kurek, M. Wasiucionek, W. Jakubowski, J.R. Dygas, Mater. Sci. Eng. **21** (1993) 70.
12. Y.P. Xiong, H. Kishimoto, K. Yamaji, M. Yoshinaga, T. Horita, M.E. Brito, H. Yokokawa, Solid State Ionics **192** (2011) 476.
13. B.D. Cullity, *Elements of X-ray Diffraction*, 1st Edition, Library of Congress (1956) Notre Dame, Indiana.
14. B. Nettelblad, B. Zhu, B-E. Mellander, Phys. Rev. B **50** (1997) 10.

5.1 Conclusion:

The solid oxide fuel cell technology is required to develop newer materials for energy generation and decreasing the working temperature which lead to the decrease of cost and an increase in working time duration. The Na_2O doped CeO_2 samples are synthesized by solid state reaction method to check their suitability as an electrolyte. The lower valence (Na_2O) doping increase the sinterability of the samples as density increases with the dopant concentration. The conductivity is not showing any appreciable change with respect to the doping concentration. The XRD pattern of samples clearly shows the presence of two cerium oxide phases. The relative density of the samples is higher than 94%. The optical band gap of the samples are in insulating range ~ 3.07 eV - 3.21 eV. The SEM images show uneven distribution of particles and the particle size is ~ 3μm. The grain size could not change with the dopants content. The conductivity is lower than the un-doped sample.

5.2 Future scope:

The rietveld refinement can be done to confirm the presence of secondary phase in the samples. Higher concentration of the dopants can also be studied to ascertain the maximum solubility of Na_2O in CeO_2. These samples can be studied for the dielectric properties since the conductivity is very low (~10^{-7} S/cm).